Physics of Fluids

RESEARCH ARTICLE | APRIL 25 2023

Hydrodynamics of body–body interactions in dense synchronous elongated fish schools

John Kelly ; Pan Yu (潘宇) ; Alec Menzer ; Dong Haibo (董海波)

Physics of Fluids 35, 041906 (2023)
https://doi.org/10.1063/5.0142950

AIP Publishing

Physics of Fluids ARTICLE scitation.org/journal/phf

Hydrodynamics of body–body interactions in dense synchronous elongated fish schools

Cite as: Phys. Fluids **35**, 041906 (2023); doi: 10.1063/5.0142950
Submitted: 18 January 2023 · Accepted: 29 March 2023 ·
Published Online: 25 April 2023

View Online Export Citation CrossMark

John Kelly, Yu Pan (潘宇), Alec Menzer, and Haibo Dong (董海波)[a)]

AFFILIATIONS

Department of Mechanical and Aerospace Engineering, University of Virginia, Charlottesville, Virginia 22904, USA

[a)]Author to whom correspondence should be addressed: haibo.dong@virginia.edu

ABSTRACT

Mechanisms for hydrodynamic benefit via fluid interactions in large planar fish schools ($n \geq 10$) are investigated by two-dimensional numerical simulations of carangiform fish swimming. It is observed that the average swimming efficiency of the 10-fish school is increased by 30% over a single swimmer, along with a thrust production improvement of 114%. The performance and flow analyses characterize the associated hydrodynamic interaction mechanisms in large dense schools leading to enhanced performance. First, anterior body suction arises from the proximity of the suction side of the flapping tail to the head of the following fish. Next, the block effect is observed as another fish body blocks the flow behind a fish. Finally, the wall effect enhances the flow of momentum downstream where the body of a neighboring fish acts as a wall for the flapping of a fish tail moving toward it. Because these primary body–body interactions are based on the arrangement of surrounding fish, a classification of the individual fish within the school is presented based on the intra-fish interactions and is reflected in the performance of the individuals. It is shown that the school can be separated as front fish, middle fish, edge fish, and back fish based on the geometric position, performance, and wake characteristics. Finally, groupings and mechanisms observed are proven to be consistent over a range of Reynolds numbers and school arrangements.

I. INTRODUCTION

Fish schooling is motivated by a variety of factors, including predator defense, reproduction, socialization, and hydrodynamic benefits.[1,2] As engineers, we are most interested in the hydrodynamics of fish schooling for its application in our underwater vehicles. Significant progress has been made in optimizing these vehicles for both speed and efficiency,[3–6] but more advancements are required in understanding fish schooling to fully optimize larger groups of them.

To understand fish schooling from a hydrodynamics perspective, many studies have utilized two-fish systems, employing two-dimensional (2D) computational simulations and experiments to investigate energetic, thrust, and stability benefits in flags,[7] flapping foils,[8–15] and undulating foils.[16–22] Utilizing side-by-side, in-line, and staggered arrangements, some mechanisms for hydrodynamic benefit from schooling were uncovered. In flapping foils, Broering *et al.*[9] showed that a large thrust benefit is gained by the upstream foil when two foils are flapping in-line. Enhancements to the downstream foil efficiency and thrust were also observed for some spacing and phase combinations in multiple studies.[10,11] In undulating foils, hydrodynamics and wake classification of two fish swimming side-by-side were investigated by Dong and Lu,[16] showing that in-phase swimming provided power saving for the system, while anti-phase swimming enhanced the forward forces generated. Maertens *et al.*[22] showed that hydrodynamic benefits can be achieved via an interaction with incident vortices from upstream fish. Khalid *et al.*[19] found that in-line swimming led to an enhancement in performance for the upstream fish due to wake splitting by the rear fish, increasing the pressure behind the upstream fish. A drafting effect benefiting the trailing fish is also observed for some conditions. These two fish studies establish some of the hydrodynamic fish–fish interactions, in addition to unique performance for leader and follower fish; however, significant progress is still required to understand hydrodynamics within entire fish schools.

Significant work has been done in extending 2-fish fluids studies into larger schools using more robust fluids models, including infinite school approximations[23–26] and multiple fish models.[27–35] Saadat *et al.* simulated an approximation for infinite foils utilizing a periodic boundary condition at the inlet, finding that hydrodynamic benefits of schooling in-line come from leading-edge suction on the trailing foil and added-mass push on the leading foil.[23] While valuable for sparse schools, the infinite school approximation prevents close proximity of the fish due to the boundary condition setup, requiring more fish in a

single domain to observe larger dense schools. Lin *et al.*[32] and Peng *et al.*[33] found stability in self-propelled foils in dense arrangements. Becker *et al.*[26] and Park and Sung[34] show that interactions with the vortex wake from previous fish can enhance performance in subsequent fish within a school. In Dai *et al.*, numerical simulations of 2D fish were leveraged to investigate energetics in schools with 2–4 fish.[27] Their results suggest that more compact arrangements achieve a lower cost of transport. Additionally, on the topic of diamond schools, Pan and Dong investigated spacing and phase in a diamond school arrangement.[28,29] They found that the dense diamond school maximized interaction between fish and attributed hydrodynamic benefits from schooling to a block effect, wall effect, body–body suction, and vortex capturing. They also identified distinct interactions for the front, edge, and back fish, with both edge fish in the diamond behaving similarly.

Hydrodynamic interaction in large fish schools has received limited attention in the literature; however, some progress in understanding has been made using lower-order models of a large number of fish in a school.[36,37] Gazzola *et al.* utilized a coupled reinforcement learning optimization of control of fish in large schools with a finite-width dipole method to model the interactions between swimmers.[36] Their work evaluated various arrangements of 100 swimmers, concluding that elongated school shapes allow for drafting and pushing to occur, improving the school's performance. It was also found that densely packed swimmers within the school gave the best opportunity to leverage interactions for performance benefit. Filella *et al.* published work that similarly uses a dipole method to approximate hydrodynamics for schools of 100 swimmers, finding that individuals in the school reached higher swimming speeds when including hydrodynamic interactions with the fish around it in the school.[37] These studies provide valuable groundwork for understanding larger fish schools; however, the dipole method used in these studies is low fidelity, and more work is needed to understand the details of flow interactions for the hydrodynamic benefits of schooling to be fully leveraged.

Biological studies of fish schooling have identified aerobic capacity, as well as anti-predator behavioral responses, essential in identifying unique spatial positioning groups of individual fish within the school.[38,39] Despite some progress in understanding individual fish performance in 2–4 fish models, no significant understanding has been reached of how positioning within a larger school affects the hydrodynamic performance of the individual fish.

In this research, we utilize an immersed boundary method-based incompressible flow solver to simulate large ($n \geq 10$) 2D fish schools in a variety of arrangements and Reynolds numbers. We investigated the resulting hydrodynamic performance, body–body interactions within the school, and wake features, giving the first high-fidelity fluid analysis within a large fish school. Additionally, we demonstrate that individual fish can be grouped based on the arrangement of their neighbors. These groupings, along with the underlying flow mechanisms, are shown to be consistent with changes in width, length, and Reynolds number. The structure of this paper is organized as follows: The methodology for the fluid solver, validation for that method, and arrangement of the schools are presented in Sec. II. The results, along with a detailed discussion of underlying hydrodynamics and the observed groupings, are presented in Sec. III. Finally, Sec. IV provides a summary of the work and its applications in the future.

II. METHODOLOGY

A. Fish-like kinematics and school configuration

To define the fish-like motion for the study, a NACA0012 foil shape is used for the equilibrium state of the fish body. Then, traveling wave kinematics are imposed on the foil, giving a resulting undulatory motion that mimics a top-down view of typical carangiform swimming. The body length is scaled to $l = 1$, and the lateral displacement is given by the following equation:

$$y(x,t) = A(x)\sin\left(\frac{2\pi}{\lambda}x - \frac{2\pi}{T}t\right), \tag{1}$$

where the position variables, x and y, are normalized by the body length such that at the equilibrium state the midline of the fish body is a flat line at $y = 0$ spanning from $x = 0$ to $x = 1$. $y(x, t)$ represents the lateral deviation from this midline position during the undulating motion. T is the wave period of the traveling wave, and λ is the wavelength, both of which are set to one. $A(x)$ denotes the amplitude of the lateral wave and is expressed by the following quadratic polynomial:

$$A(x) = a_2x^2 + a_1x + a_0, \tag{2}$$

where the coefficients are determined to be $a_0 = 0.02$, $a_1 = -0.08$, and $a_2 = 0.16$. These were determined by previous experimental data[40] and have been used in previous 2D computational studies of fish swimming.[28,41] The wave amplitude envelope and the resulting midline sequence through a cycle of motion are given in Fig. 1(a).

To determine the arrangement of fish within the school, the basic dense diamond school is utilized. The diamond school shape has been identified by previous studies to be the most energy efficient for a small number of fish,[1,42,43] and most recently, the dense school has been identified as the highest efficiency,[36] particularly for the diamond configuration.[28] To enable studies of many fish in a school, we utilize the dense diamond as a basic sub-unit of the larger school. This allows us to observe the most efficient arrangements of fish. Additionally, the highly compact dense diamond maximizes interaction between fish within the school. Utilizing this configuration, we capture all the fish–fish interactions experienced by schooling fish. In keeping with the findings of the previous study, the dense diamond is defined in Fig. 1 as $D = 0.4$ and $S = 0.4$. To construct larger schools, additional sub-units of the dense diamond are appended to the previous school. The elongated school is shown in part (b), with additional dense diamond

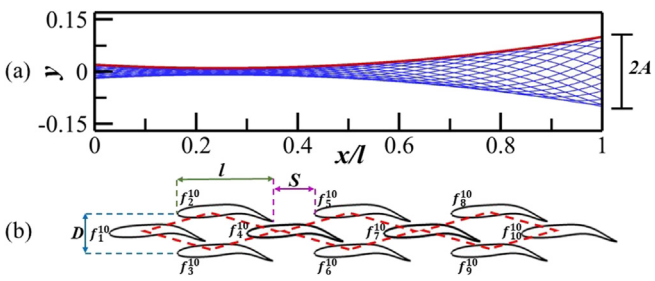

FIG. 1. (a) The traveling wave amplitude of a carangiform motion (red line) and the motions of the fish body mid-line during one tail-beat period (blue lines). *A* denotes the amplitude at the tail tip. (b) A schematic of an elongated dense diamond fish school with 10-fish and the definitions of its spatial arrangement and fish numbering. The diamond sub-unit is shown in red.

sub-units added in line to create a 10-fish school. To distinguish the fish within the school, fish are numbered top to bottom, left to right, as shown in Fig. 1(b). Throughout the text, the notation f_a^b is used, where a is the fish number and b is the total number of fish in the school.

B. Numerical methods and case setup

In this study, the 2D unsteady viscous incompressible Navier–Stokes equations, written in index form as

$$\frac{\partial u_i}{\partial x_i} = 0; \quad \frac{\partial u_i}{\partial t} + \frac{\partial u_i u_j}{\partial x_j} = -\frac{\partial p}{\partial x_i} + \frac{1}{Re}\frac{\partial u_i^2}{\partial x_i \partial x_j}, \tag{3}$$

govern the flow. In the equations, p is pressure, u_i denotes Cartesian velocity components, and Re is the Reynolds number, given by the equation $Re = \frac{U_\infty l}{\nu}$, where U_∞ is the forward swimming velocity, l is the length of the body, and ν is the kinematic viscosity of water. An in-house immersed boundary method-based finite difference flow solver is employed to solve the equations, which are discretized spatially using a cell-centered collocated arrangement of the primitive variables and integrated in time using a fractional step method. This method has been successfully employed in previous biological swimming studies[44–46] and bio-inspired canonical problems,[47–51] and has been previously validated extensively.[48,52,53] More details can be found in Refs. 54 and 55.

A representative Cartesian grid is shown in Fig. 2(a) for the baseline case of a 10-fish school. The domain employed is $10l \times 20l$, with the domain length growing for each longer school. Around the body, a fine mesh region is employed with a minimum grid spacing of $0.0035l$. The resulting grid is 1696×704, giving about 1.2×10^6 total grid points. The boundary conditions are also shown, with the velocity boundaries defined by an inlet boundary condition with U_∞ from the left, an outlet boundary condition on the right to allow vortices to exit the domain without reflection, and zero gradient upper and lower boundaries with U_∞ to enforce free stream conditions. A grid independence study was completed on this grid, shown in Fig. 2(b). In the figure, the net force in the −x direction is shown for the back fish using each of the grid sizes, where the coarse mesh has a minimum grid size of $0.0051l$ and the fine mesh has a minimum grid size of $0.0025l$. The average and peak C_x values, calculated as $C_x = \frac{F_x}{0.5\rho U_\infty^2 l}$, are within 2% for the nominal and fine grids, so the nominal grid is determined to be sufficient for the study.

To further validate the computational solver for multi-body interacting flows, the experimental work of Dewey *et al.*[56] is reproduced using the solver to verify its accuracy. In this experiment, Dewey studies two flapping foils in a side-by-side configuration, varying their phase difference (ϕ) at the Strouhal number of maximum efficiency (0.25) and a Reynolds number of 4700. The foils span the entire depth of the water channel, mitigating their 3D effects and allowing a 2D computational approximation to compare closely with their results.

The results from the experimental data along with the computational comparison from our solver are shown in Fig. 3. In part (a), the streamwise force coefficient for experimental data is given by the points, as calculated via the equation shown in their paper, with the experimental error shown by the error bars, along with the computational data shown by the lines. From this, we see that almost every data point is within the experimental error. All points outside of the experimental error occur at very low values of C_x, where the experimental error range, which is given as a percentage by Dewey *et al.*, is very small. This confirms the validity of our solver in calculating the hydrodynamic performance in multi-foil interacting systems. Parts (b) and (c) contain the vorticity and time-averaged velocity from the computational data for the highest thrust-producing case, $\phi = \pi$. In the figure, the vortices shed from each foil are seen advecting away from the center plane, resulting in the divergence of the pairs of jets behind the foils. This lateral advection and jet divergence are also observed in the experimental results of Dewey *et al.*, with very similar vortex structures shown, further validating our computational solver for vortex structures in unsteady multibody interacting fluid flows in the biological regime.

C. Performance definitions

To solve for the hydrodynamic forces, F_x and F_y, the solver directly integrates the projected surface pressure and shear force over each body, expressed as

$$F_x = -\int_S (-pn_x + \tau_{xi}n_i)dS, \quad F_y = \int_S (-pn_y + \tau_{yi}n_i)dS, \tag{4}$$

where the indices $i = 1, 2$ represent the x and y direction, τ_{ij} is the viscous stress tensor, and n_i represents the ith component of the unit

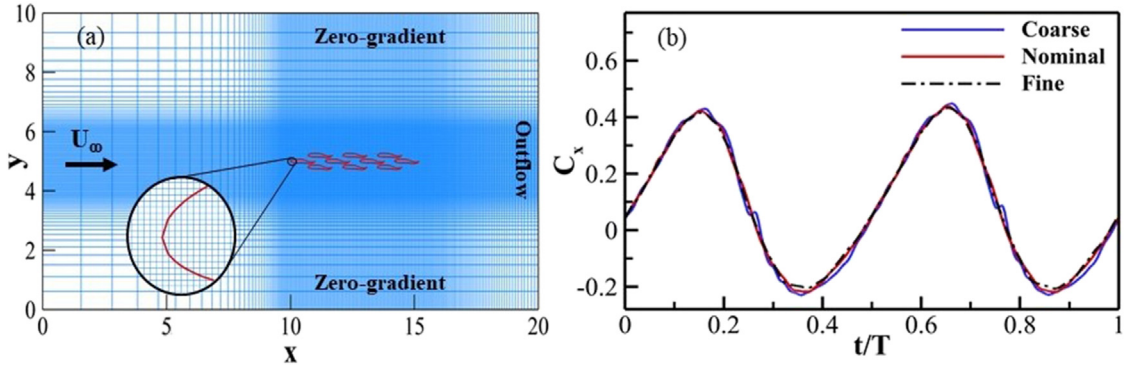

FIG. 2. (a) Schematics of the computational domain, Cartesian grid, and boundary conditions, with a detailed inset of the grid density on the body. (b) Comparison of the instantaneous net force coefficient of the last fish in the 10-fish school between the coarse, medium, and fine mesh.

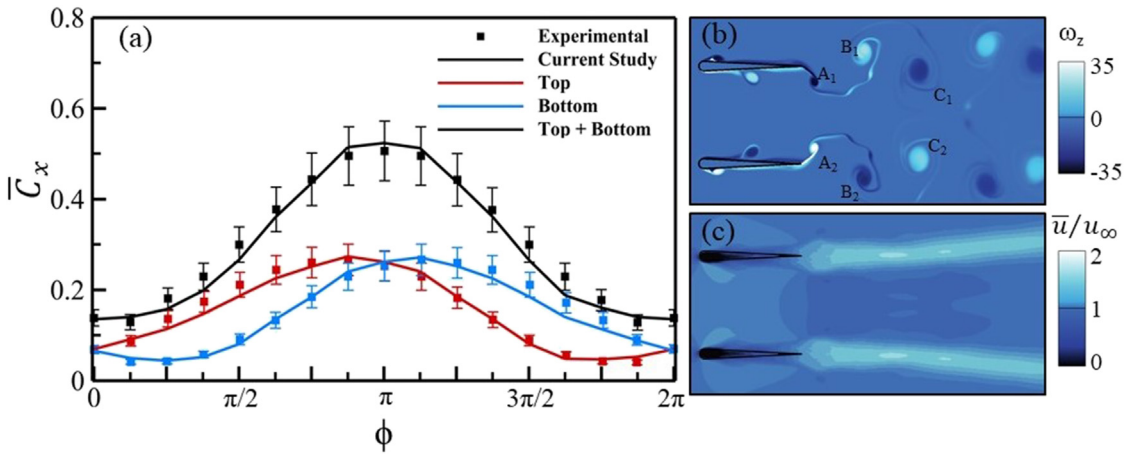

FIG. 3. (a) Streamwise force coefficient of experimental results with error bars, along with the current computational study. Vorticity (b) and average velocity (c) from the computational results for $\phi = \pi$.

normal vector on element dS. Note that F_x is defined in the $-x$ direction, such that positive F_x indicates a net thrust and negative F_x indicates a net drag. The resulting force coefficients C_x and C_y are computed by

$$C_x = \frac{F_x}{0.5\rho U_\infty^2 l}, \quad C_y = \frac{F_y}{0.5\rho U_\infty^2 l}. \tag{5}$$

Thrust and drag are then computed by further separating the pressure and viscous stress components of F_x by their sign. The thrust on the body then consists of the sum of the forward force on the body, resulting in the thrust coefficient given by

$$F_T = \frac{1}{2}\left(-\int_S -pn_x dS + \left|\int_S pn_x dS\right|\right) + \frac{1}{2}\left(-\int_S \tau_{xi} n_i dS + \left|\int_S \tau_{xi} n_i dS\right|\right), \tag{6}$$

$$C_T = \frac{F_T}{0.5\rho U_\infty^2 l}. \tag{7}$$

The total power is defined as the rate of the output work done by the fish to complete its motion. It is given mathematically by

$$P_u = \int_S (-pn_i + \tau_{ij} n_j)\Delta u_i dS, \tag{8}$$

where Δu_i is the velocity of the element dS relative to its surrounding fluid in the ith direction. The coefficient of power can then be calculated as

$$C_{pw} = \frac{P_u}{0.5\rho U_\infty^3 l}. \tag{9}$$

From these coefficients, we define a modified Froude efficiency η consistent with previous studies:[28,41]

$$\eta = \frac{U_\infty \overline{F_t}}{U_\infty \overline{F_t} + \overline{P_u}} = \frac{\overline{C_T}}{\overline{C_T} + \overline{C_{pw}}}, \tag{10}$$

where the overline ($\bar{}$) denotes values averaged over a cycle of motion.

III. RESULTS

For the study, the undulating swimmers remain in a fixed position with no transnational or rotational degrees of freedom. We find the steady-swimming condition by obtaining the flow parameters that results in a cycle-averaged net force of 0 for the single swimmer. The Reynolds number Re is initially chosen to be 1000. This is consistent with[28,49] and corresponds to a higher Reynolds number in three dimensions.[42] In this Reynolds number regime, the viscous effect are small while coherent vortex structures are still maintained.[57] The effect of changing the Reynolds number is presented later in the study. With the fixed Re, we simulate a range of flow velocities to find the steady-swimming condition. This results in a steady-swimming Strouhal number ($St = 2fA/U_\infty$) of 0.43. We summarize all flow and kinematic parameters in Table I. A is a result of the equations given in Fig. 2. The body length l and the wavelength λ are both set to one.

For the parameters chosen in this work, the time-averaged thrust of a single fish is $\overline{C_T} = 0.22$, the undulating power coefficient is $\overline{C_{Pw}} = 0.28$, and the associated propulsive efficiency is $\eta = 0.44$. Specifically, the swimmer suffers drag at the snout, while the tail generates most of the thrust and power consumption. The shedding vortices behind the fish form a 2S wake. More details about a single swimmer's hydrodynamic performance and flow field can be found in Pan and Dong.[28,29]

A. 10 Fish school hydrodynamics

To observe larger fish schools, a baseline school is studied, configured like a series of 4-fish school diamonds as shown in Fig. 1. The resulting cycle-averaged net force, along with the efficiency, thrust, and power consumption for individual fish, along with the school

TABLE I. Parameters used in this study.

Re	A	Λ	l	St	N_{fish}
1000, 2000, 4000	0.1	1.0	1.0	0.43	10, 16, 23

TABLE II. Cycle-averaged performance of individuals in 10-fish school, as labeled in Fig. 1.

	f_1^{10}	f_2^{10}	f_3^{10}	f_4^{10}	f_5^{10}	f_6^{10}	f_7^{10}	f_8^{10}	f_9^{10}	f_{10}^{10}	f_{avg}^{10}
$\overline{C_T^*}$	1.775	2.215	2.215	2.266	2.363	2.363	2.196	2.119	2.122	1.831	2.147
$\overline{C_{pw}^*}$	1.931	1.113	1.112	1.856	1.057	1.057	2.022	1.016	1.012	0.949	1.312
$\overline{C_x}$	0.067	0.090	0.090	0.13	0.084	0.084	0.100	0.047	0.048	0.085	0.083
η^*	0.953	1.384	1.384	1.112	1.446	1.446	1.046	1.410	1.412	1.368	1.296

averages, are shown in Table II, where * indicates values normalized by the solo swimmer. The performance of the school, in both C_x and η, is significantly higher than a single fish, with an average efficiency of 57.3%, a 30% improvement over the single fish swimming value of 44.2%, affirming that hydrodynamic benefit is gained by the fish through dense schooling. In comparing results with Pan and Dong,[28] the larger school sees a further efficiency benefit of 9% from schooling compared to the 4-fish dense diamond school.

Efficiency is gained from schooling by every individual, with the least gain for f_1^{10} at the front of the school and the most gain for f_5^{10} and f_6^{10} in the middle. Symmetry in the cycle-averaged performance is also seen across symmetric fish in the school, with f_2^{10} and f_3^{10}, f_5^{10} and f_6^{10}, and f_8^{10} and f_9^{10} having values within 1% of each other.

Next, the force coefficients and power consumption are given in Figs. 4(a)–4(d). From the figures, a 2-peak cycle is shown, with maximum C_T and C_y magnitudes occurring at $t/T = 0.2$ near the end of the left stroke, and again at $t/T = 0.7$ near the end of the right stroke of the tail. To investigate the flow within the school, the vorticity for the maximum and minimum C_x is given in Fig. 5 (Multimedia view), along with the flow for a complete cycle of motion. Major vortices are labeled using $V_{L/R}^{\sharp}$, where the top number indicates the fish where the vortex originates, and the letter on the bottom indicates that it is generated during the left or right stroke. During each half stroke, the trailing edge vortex is shed off the tail region of the fish. For all but f_{10}^{10}, the tail also interrupts the shear layer of the next fish in the school, causing a small induced vortex which has been discussed at the back of diamond schools.[29] The shed vortex then advects downstream. An example is shown by V_L^1 and V_R^1, where each is seen advecting along the body of the next fish after shedding from the trailing edge vortex of f_1^{10}. The induced vortices can be seen along the body of f_2^{10} and f_3^{10}.

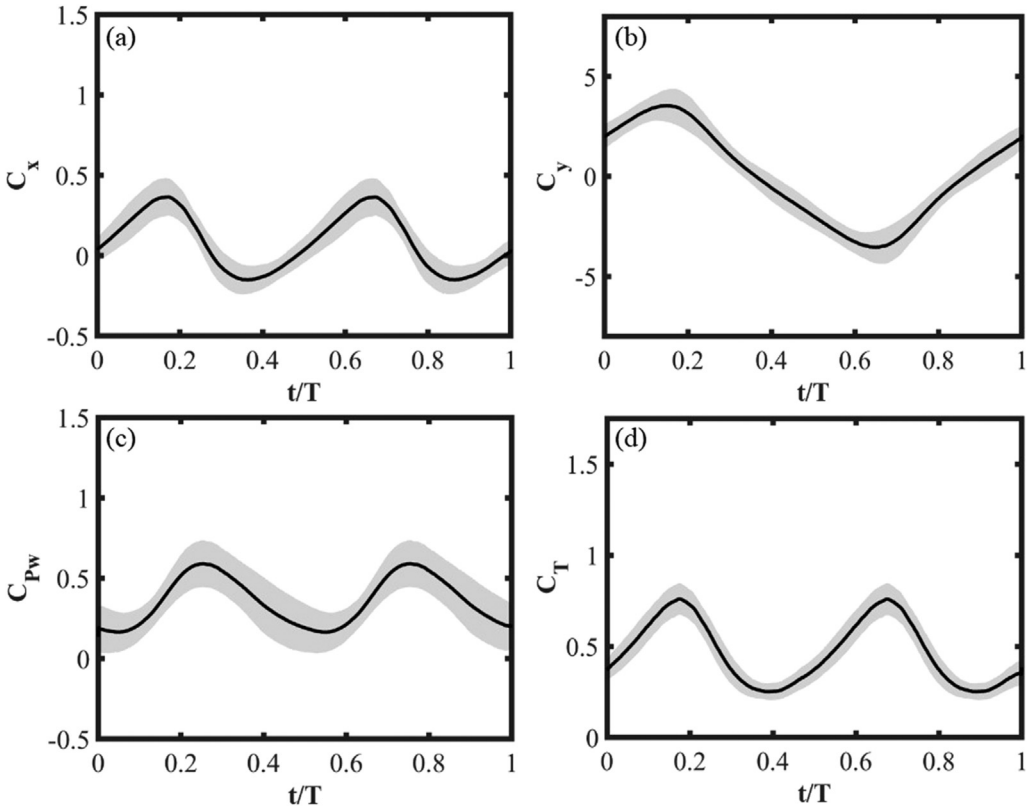

FIG. 4. 10-fish school average C_x (a), C_y (b), C_{pw} (c), and C_T (d) displayed over a cycle of motion, with the standard deviation shaded.

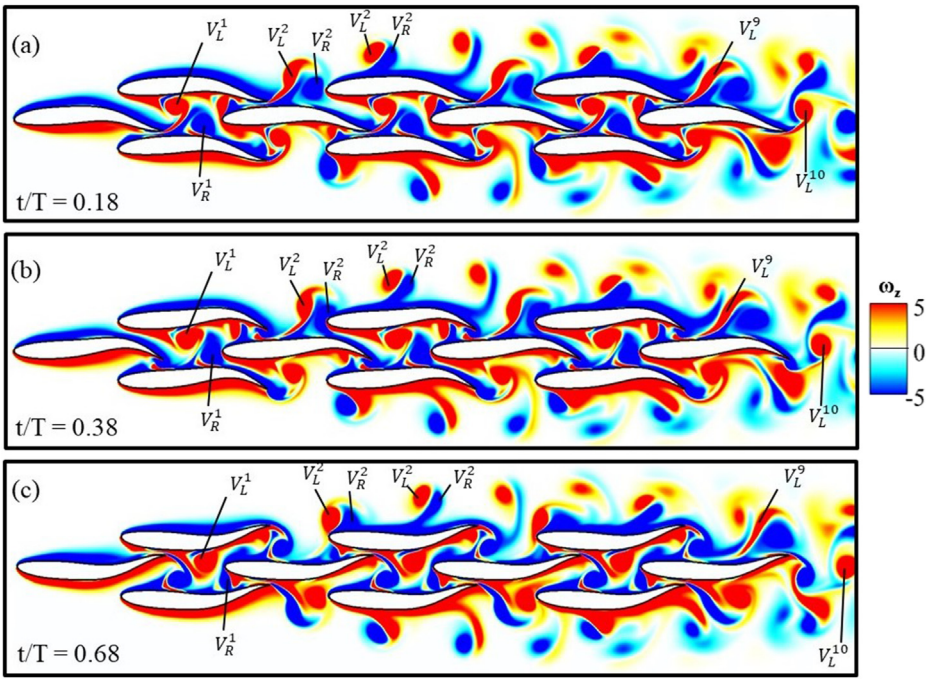

FIG. 5. Vorticity (a)–(c) at $t/T = 0.18$, 0.38, and 0.68. Key vortices are noted. Multimedia view: https://doi.org/10.1063/5.0142950.1

For the fish along the mid-line, the vortex is then captured by the channel of surrounding fish and intercepts the head of the next fish behind it. On the edges of the school, the vortices form a pair and advect laterally outside the school after intercepting the next fish in line, as shown by V_L^2 and V_R^2. For f_{10}^{10} at the back of the school, a single vortex (V_L^{10}) shed in each half stroke with no subsequent interactions.

To summarize, the primary vortex structures are given in Fig. 6, with the major vortices represented along with the fish bodies. Each plot shows the major vortices relevant to the body shown in orange. First, f_1^{10} is characterized by no oncoming vortices to interact with and the vortices shed from the tail are contained completely by the channel created by f_2^{10} and f_3^{10} (a). Next, all the fish along the edges of the school are characterized by the lateral advection of the vortex pair shed at the tail, similar to the edge fish vortex pattern observed in the dense diamond school in Pan and Dong[28] (b). Apart from the front-edge fish, they have an incident vortex pair from the previous edge fish. Additionally, with the exception of the back-edge fish, there is another edge fish partially blocking the shed vortex from advecting in the streamwise direction. The fish along the midline of the school have a vortex shed from its tail, which is entirely constrained to the channel created by edge fish around it (c). The subsequent fish behind it blocks the streamwise advection of the vortex coming from its tail. Finally, f_{10}^{10} similarly has a vortex incoming from the channel in front of it, but behind it only generates a single vortex that is unobstructed as it flows downstream (d). Additionally, since there is no additional edge fish to disrupt the propagation of the vortex pair next to it, the pair coming from the neighboring back-edge fish also interacts with the tail portion of f_{10}^{10}.

The wake structure is shown in Fig. 7, with the major components labeled in the vorticity plot in (a), the lateral velocity in (b), and the cycle-averaged streamwise velocity in (c). The wake is shown to have a typical reverse Bérnard–von Kármán (rBvK) wake core behind

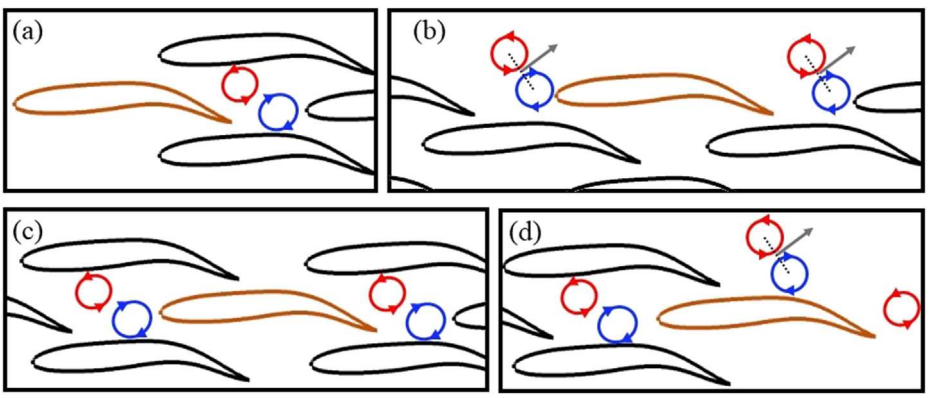

FIG. 6. Schematic of primary vortex interactions based on arrangement of neighboring fish.

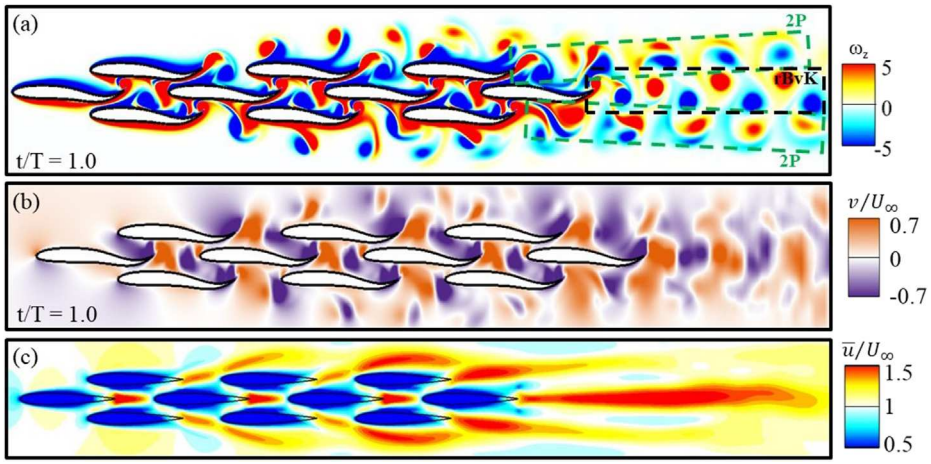

FIG. 7. Vorticity (a), lateral velocity (b), and time-averaged streamwise velocity (c) demonstrating the wake structure in the 10-fish school.

f_{10}^{10}, noted in black at the center of the wake. On the edges, two 2P wake pairs are observed in green, owing to the lateral proximity of f_8^{10} and f_9^{10}. This overall structure matches the wake pattern shown by the dense diamond school in Pan and Dong.[28,29] The additional vortices shed by the other fish along the edge of the school either combine with the wake structure present or are mostly dissipated before reaching the back of the school, creating a similar wake to the synchronous dense diamond school. The angle of the 2P vortex streets is more narrow than the 4-fish school results, owing to the weaker vortices from previous edge fish creating a channel for the later vortex wake, trapping it in a more narrow space as can be seen in V_L^9 in Fig. 5. Additionally, the lateral spacing between the positive and negative vortices in the rBvK wake is wider than the in-phase diamond school, which is noted in Pan and Dong[29] to correlate with higher C_x in the school. In the cycle-averaged velocity (c), small but increasing jets are observed along the edge of the school, originating from an edge fish and occurring along the subsequent fish body. Behind the school, a single narrow long jet is observed, correlating with the rBvK wake in the vortex wake. Additionally, two short jets occur behind the edges of the school, corresponding to the 2P vortex structures discussed previously.

Next, the force vectors are plotted along the surface of each fish body at the instance of peak thrust during the cycle of motion, $t = 0.18T$, in Fig. 8(a). The forces with a net thrust production are shown in red, and the net drag production is shown in blue. From the figure, a surprising result is seen among many of the fish. In addition to the expected higher thrust output near the tail, all except the front and top-edge fish have suction thrust on the head portion of the body. For example, a drag-producing region is observed on the front half of the top of all edge fish along the top of the school (f_2^{10}, f_5^{10}, and f_8^{10}), whereas all other fish have some thrust production in that region. On the same fish, there is a high thrust region on the top of the tail portion that also occurs only in f_{10}^{10}. The front half of f_{10}^{10} has the same pattern as the middle fish, f_4^{10} and f_7^{10} with a high thrust region in the front followed by a drag-producing region around the middle. The bottom-edge fish have a large thrust-producing region in the first half of the top edge. For the edge fish, the top and bottom are different because

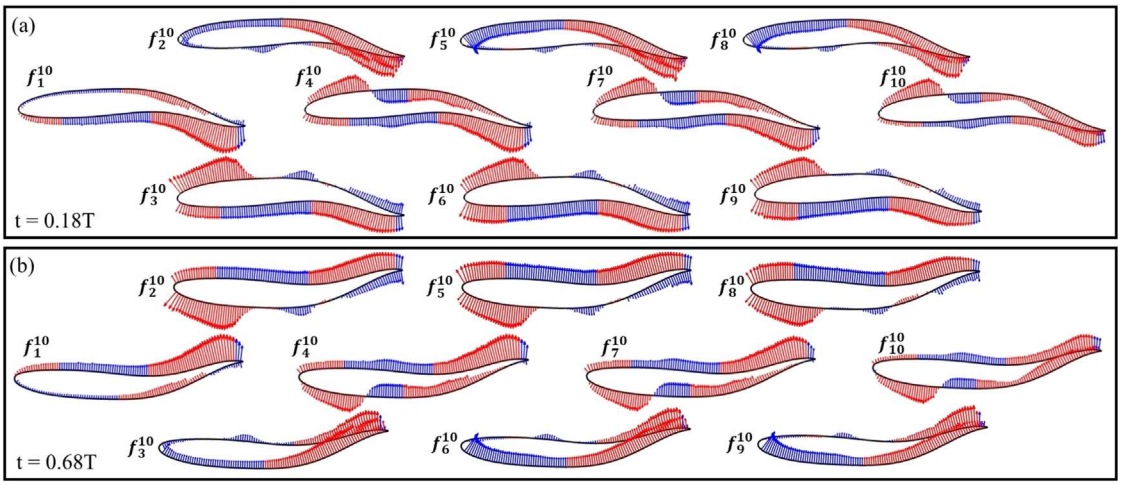

FIG. 8. Surface force vectors along each fish in the 10-fish school at the peak thrust production, $t/T = 0.18$ (a) and $t/T = 0.68$ (b). Blue denotes net drag, and red denotes net thrust on the surface.

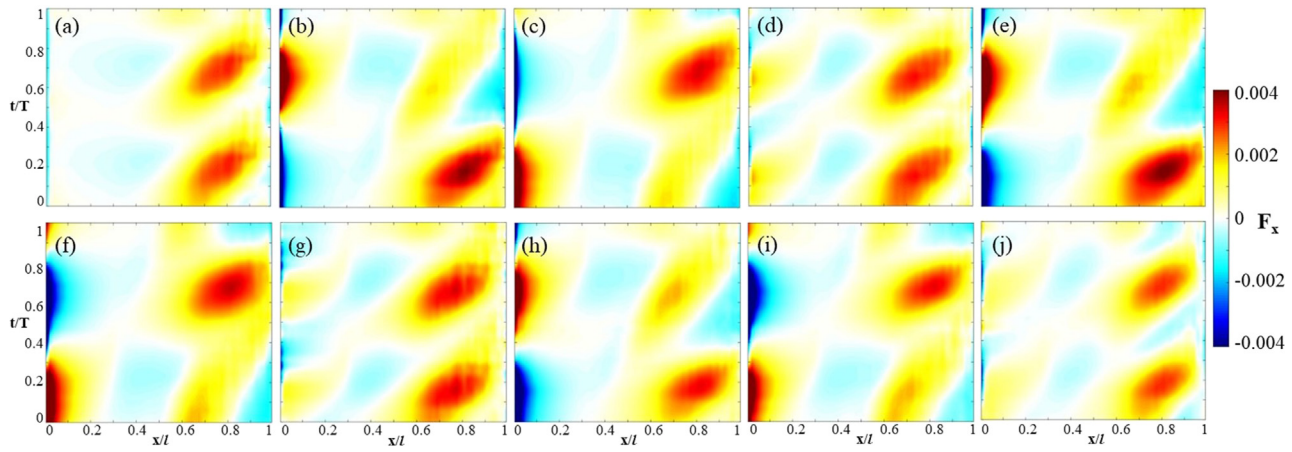

FIG. 9. Spatiotemporal forward force $F_x = -(-pn_x + \tau_{xi}n_i)$ along the fish body through one cycle of motion for (a) f_1^{10}, (b) f_2^{10}, (c) f_3^{10}, (d) f_4^{10}, (e) f_5^{10}, (f) f_6^{10}, (g) f_7^{10}, (h) f_8^{10}, (i) f_9^{10}, and (j) f_{10}^{10}.

they are in different parts of the cycle, with the top-edge tail flapping in toward the middle of the school and the bottom-edge tail flapping away from the middle of the school. The top edge is in peak tail thrust production at $t/T = 0.18$, while the bottom edge is in peak head thrust production corresponding to $t/T = 0.68$ in the figure. The school shape is symmetric, however, so the bottom-edge fish experience the tail and head thrust production times opposite of the top-edge fish. The opposite can be seen at $t = 0.68T$ in part (b). At this time, the top edge has suction force at the head, and the bottom edge has a larger net thrust at the tail. The fish along the mid-line have a mirrored performance to $t = 0.18T$.

Next, the spatiotemporal force $[F_x = -(-pn_x + \tau_{xi}n_i)]$ for each fish in the school is shown in Fig. 9. The overall pattern of two zones of high thrust near the tail, shown in red, corresponding to the end of the left and right strokes, is consistent with the previous study of Pan *et al.*[29] As expected, the front half of the front fish f_1^{10} shows unique performance, with a consistent drag zone on the tip through the entire cycle (a). The back half of the front fish, however, is very similar to the other mid-line fish (f_4^{10}, f_7^{10}, and f_{10}^{10}), with two consistent zones of high thrust near the back. The subsequent mid-line fish also have a smaller thrust zone near the head twice each cycle. The back fish has a smaller high thrust zone during its two peaks. Most unique is the fish along the edge of the school (f_2^{10}, f_3^{10}, f_5^{10}, f_6^{10}, f_8^{10}, and f_9^{10}), which have a single high thrust and single high drag phase on the front. Additionally, unlike the two high thrust regions on the back observed by all other fish, there is only one region of high thrust. The high thrust on the tail occurs when the tail is flapping inwards toward the school, and the performance for symmetric fish ($f_{2/3}^{10}$, $f_{5/6}^{10}$, and $f_{8/9}^{10}$) is similar, with the half cycled performances flipped.

The spatiotemporal power consumption $Pw = -(\bar{\bar{\sigma}} \cdot n) \cdot u)$ for each fish in the school is shown in Fig. 10. The overall pattern of two zones of high power consumption near the tail, shown in red, corresponding to the end of the left and right strokes, is consistent with the previous study of Pan *et al.*[29] There are some differences in power

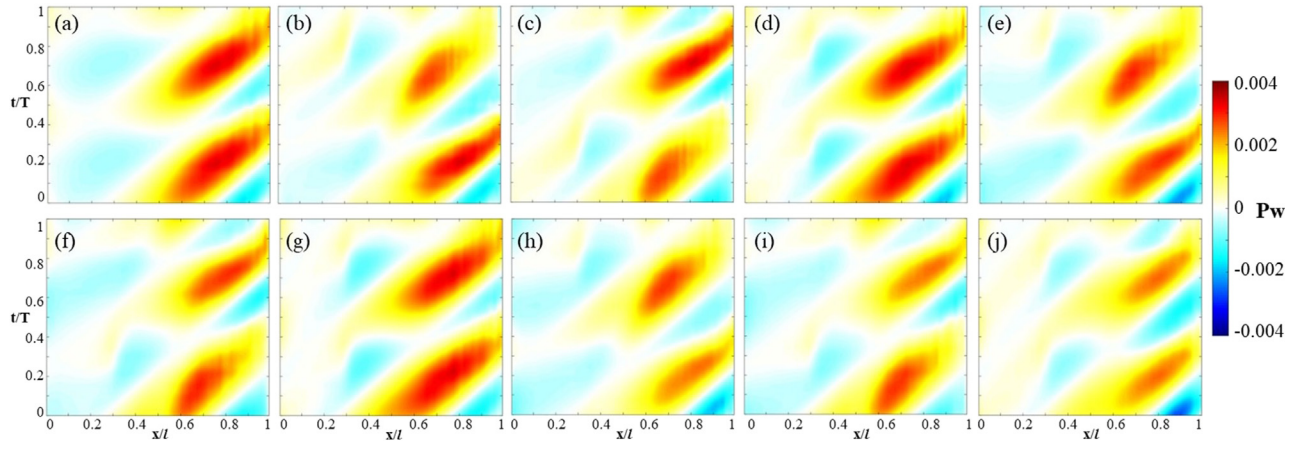

FIG. 10. Spatiotemporal power consumed $Pw = -(\bar{\bar{\sigma}} \cdot n) \cdot u$ along the fish body through one cycle of motion for (a) f_1^{10}, (b) f_2^{10}, (c) f_3^{10}, (d) f_4^{10}, (e) f_5^{10}, (f) f_6^{10}, (g) f_7^{10}, (h) f_8^{10}, (i) f_9^{10}, and (j) f_{10}^{10}.

consumption between individual fish. First, the fish along the edge of the school has one small and one large power consumption zone near the tail, with the smaller and larger zone corresponding to the tail flapping away from and toward the school, respectively. Additionally, the back fish, f_{10}^{10}, has smaller high-power consumption regions for both the left and right strokes.

1. Anterior body suction

Next, the body–body interactions are studied in detail. From the works of Pan and Dong,[28,29] a few primary body–body interactions within the dense diamond school have been discussed. Within the dense diamond study, the block effect, wall effect, and anterior body suction effect are shown to be dominant body–body interactions in determining the performance of the individual fish in the school.

To begin, the anterior body suction effect is investigated in detail. This effect is shown in Pan and Dong[29] to occur from the low-pressure suction that is generated on the tail of one fish interacting with the head of the fish behind it. In the paper, the effect is discussed within the context of the back fish of the diamond, which saw a moderate suction force on its head when the body phases are matched. To investigate the effects of this throughout the school, the anterior portion of the body, defined as the first 30% of the body length, is observed through the cycle of motion. The net force is plotted in Fig. 11, with the superscript a denoting the anterior portion of the body only. Note that only the top-edge fish are included in the figure, as it has already been shown that the bottom-edge have the same results due to symmetry. Additionally, the pressure contour is shown at $t/T = 0.25$ (a) and $t/T = 0.75$ (b). The mid-line fish all show two peaks and two troughs in f_x^a, whereas the fish along the edge of the school have a single peak and trough of significantly higher magnitude.

The reason for this can be seen in Fig. 11(b). In this time step, the top-edge fish are experiencing peak thrust from the anterior body suction. The bottom-edge fish, on the other hand, are near the lowest point in their anterior net force. This can be seen using the example of the front fish (f_1^{10}). The front fish tail has created a low-pressure suction and high-pressure pushing on each side of its tail. On the suction side, the top-edge fish (f_2^{10}) is benefiting heavily from interacting with this low-pressure suction zone, gaining a large net forward force on its anterior. Conversely, the high-pressure side of the front fish also interacts with f_3^{10}, creating a large drag on its anterior portion. This effect also explains the high-thrust zones at the head seen in Fig. 9 where the mid-line fish have two small thrust and drag zones and the edge fish has one large thrust zone and one large drag zone on its anterior. This effect can be seen all along the edge fish on the top and bottom of the school in Fig. 11(a) and is expected to occur any time the suction side of a tail is near the head of another fish. In the middle fish, some net suction on the anterior is still observed, similar to the back fish in the diamond school noted by Pan and Dong.[29] This occurs due to similar suction and pushing as the edge fish, but because it has a fish on either side of it, the effects occur simultaneously. The low- and high-pressure regions on the anterior largely cancel out, leading to a much smaller net effect. The net effect is still suction on the anterior because the

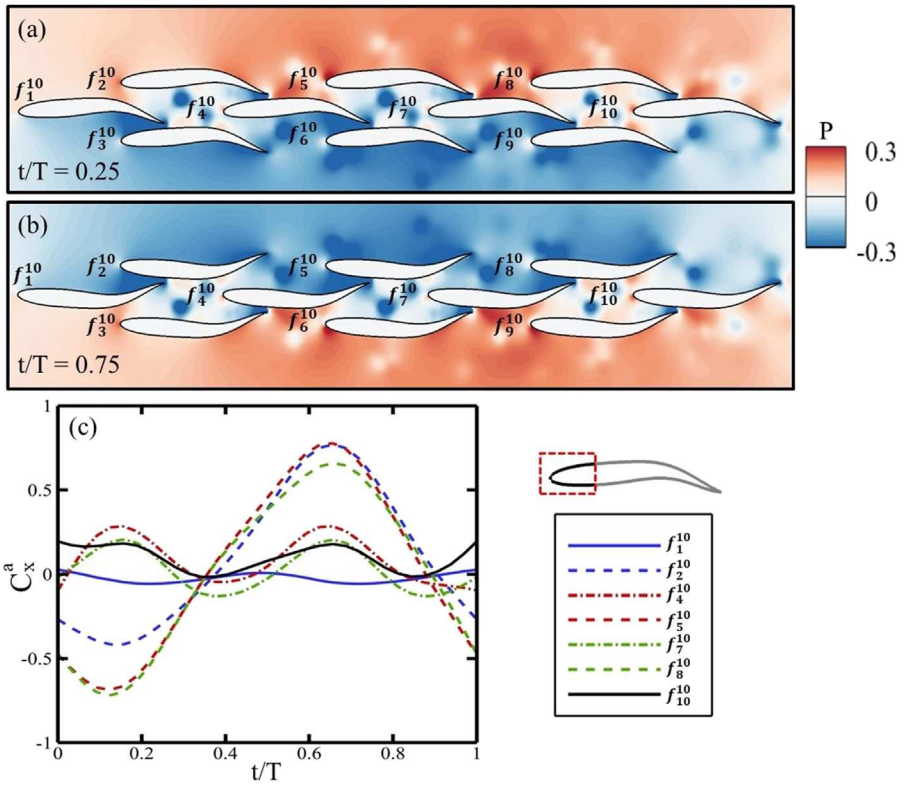

FIG. 11. Anterior body suction effect shown via pressure contour [(a) and (b)] and anterior net force (c) over a cycle of motion for each fish. Anterior fish body is defined as the first 30% of the body, as shown.

low-pressure tail is much nearer to the head of the fish than the high-pressure tail. This allows the low-pressure zone to be more dominant around the anterior, leading to the smaller net suction observed in the middle and back fish. An example of this is seen in Fig. 11(a), where f_4^{10} has mostly low-pressure around its head but is not as dominant as the previously discussed edge fish. The low-pressure from f_3^{10} and high-pressure from f_2^{10} are largely canceling out, but the head of f_4^{10} is significantly closer to the tail of f_3^{10}, meaning the low-pressure is more dominant on the body. The results of this suction can be seen in Fig. 8(a). In the figure, the mid-line fish are all experiencing moderate anterior body suction, focused around the top-edge of the fish. The bottom-edge fish are in a high anterior body suction state with high net force around the head, and the top-edge fish are in the opposite state, with high drag around the head resulting from high-pressure in front of them. Throughout this motion, the power consumption remains similar between groups on the anterior, but the front and edge fish consume less than the middle and back. Because of this, the edge fish have a more distinct cycle of high and low net force on the anterior. The low anterior thrust occurs when the tail is flapping into the school where the anterior is low net force, and subsequently low efficiency, and the high anterior thrust occurs when the tail is flapping away from the school, where the net force is high and the power consumption has not significantly increased, so the efficiency is significantly higher.

2. Block effect

The block effect is shown in prior research[28] to occur when the flow behind a fish body is blocked by another body, leading to an increase in pressure between the fish and increasing the performance of the front fish. In the context of their dense diamond school, it was demonstrated in the front fish when adding the back fish to the school, with the channel of edge fish present to block the flow from propagating laterally. Also, it was shown that in the blocking effect the flow of the vortices is prevented in the downstream. Within the context of the large school, the block effect is also observed. From the observations of the vortex structure in Fig. 5, we know that the vortices behind f_1^{10}, f_4^{10}, and f_7^{10} are blocked in their downstream propagation and f_2^{10}, f_3^{10}, f_5^{10}, and f_6^{10} also have partial blocking of the vortex pairs from the downstream.

To investigate the effects further, the cycle-averaged x-velocity is shown in Fig. 7(c), and the cycle-averaged pressure distribution is given in Fig. 12(a). From the figure, a similar but stronger jet arrangement is shown compared to the dense diamond. The edge fish, except the back-edge, only see a small momentum-carrying jet behind them, and a larger one occurs at the head of the next edge fish, owing to the partial blocking of the flow by the next edge fish. This corresponds with a higher pressure than is observed behind the fish, observed in Fig. 12(a), giving further evidence of the presence of a partial block effect occurring along the edge of the school. Additionally, the same interrupted pressure zone shape observed in Pan and Dong[28] is observed in the channel behind the front and middle fish. Unsurprisingly, the block effect continues to occur in the channel for each of these fish. Unexpectedly, this effect is not limited to blocking by a single fish. This is shown more clearly in Figs. 12(b) and 12(c), which shows the cycle-averaged pressure profile at $0.1l$ behind each fish along the mid-line and top edge of the school. The pressure continues to rise going from the back of f_7^{10} to f_4^{10} to f_1^{10}. This can be explained by the further blocking of the fluid flowing down the channel. For f_4^{10}, there is both f_7^{10} and f_{10}^{10} in the channel behind it, leading to a further increase in pressure compared to just one fish blocking the flow. This enhanced block effect is observed along the middle channel, but also in a much weaker form for the edge fish, where the pressure behind f_2^{10} is increased slightly compared to f_5^{10} because of the presence of more fish behind it. The effect of this is significantly lessened, however, because of the lack of a channel containing the flow, so much of the fluid flows laterally around the subsequent blocking fish, as seen in the jets of Fig. 7(c).

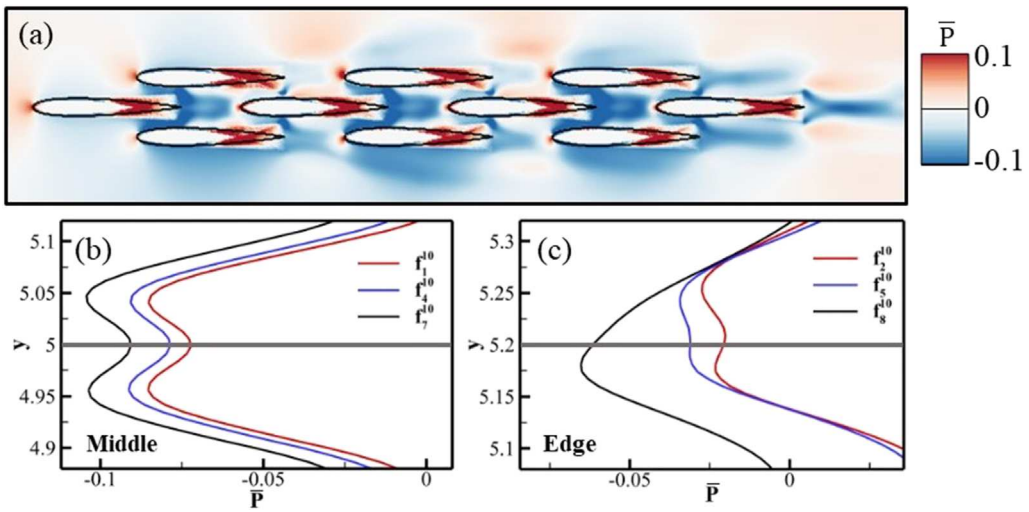

FIG. 12. Demonstration of the block effect utilizing the cycle-averaged pressure (a). The cycle-averaged pressure at $0.1l$ behind each fish tail for the mid-line fish (b) and top-edge (c) fish are also shown, with the y position of the fish marked in gray.

3. Wall effect

Many previous studies[56,58–60] have shown that foils oscillating near a solid boundary or next to another foil in anti-phase, providing a wall-like boundary in the other foil body leads to an increase in thrust with only a slight increase in power consumption. Additionally, this effect was observed in Pan and Dong[28] for a dense diamond fish school, with the tail edge of the fish breaking the stability of the shear layer on the "wall" fish. The same pattern of vortex pairs shedding reported by Pan is seen in the flow behind edge fish within the 10-fish school. This is shown along the edge of the school in Fig. 5(a), where the vortex pair V_L^2 and V_R^2 are very similar to the flow structure of the wall effect in the dense diamond reported previously. The wall effect occurs any time the tail of a fish flaps close enough to the body of another fish for the fish body to create the effect of a "wall" near the tail of the previous fish. This occurs during half of the strokes for fish along the edge of the school, and both strokes along the mid-line, except f_{10}^{10}. Along the edge, the wall effect only occurs when the tail flaps toward the center of the school. By flapping near a wall, the lateral momentum generated by the tail motion is redirected by the wall downstream. To demonstrate this effect, the normalized x-velocity is shown in Fig. 13(a). At this time step, the bottom-edge fish are flapping away from the school and the top-edge fish are flapping toward the school. From this, we expect the top-edge fish to experience a wall effect while the bottom-edge fish does not. This is evident from the velocity zones behind each of the fish, where the top-edge fish has a temporary jet of fluid flow downstream, indicating high momentum gained by the fish via Newton's third law. The fish along the bottom, on the other hand, has no high momentum region.

To compare wall effects among the fish, the total momentum of the instantaneous jet behind the tail, r_x, is summed, and the results are given in Fig. 13. From the figure, the fish without any wall effect (f_3^{10}, f_6^{10}, f_9^{10}, and f_{10}^{10}) have significantly less momentum at the tail. As expected, the top-edge fish (f_2^{10}, f_5^{10}, and f_8^{10}) have the highest momentum, and the fish with smaller momentum jets due to blockage from the middle channel (f_1^{10}, f_4^{10}, and f_7^{10}). The discrepancy between the top- and bottom-edge fish explains the single high thrust region on the edge fish tail observed in Fig. 9, while all the other fish had two zones of similar thrust at the tail. Behind the front (f_1^{10}) and middle (f_4^{10}) fish, similar high-momentum jets are observed, however, they are interrupted by the subsequent body inside the channel. Because of this, the benefit from the wall effect is lessened for these front and middle fish compared to the edge fish. This explains the weaker thrust region for all but the edge fish observed in Fig. 9.

B. Classification of individual fish

All the hydrodynamic interactions between swimmers and their wakes are based on the spatial arrangement of neighboring fish. Because of this, the fish within the large school can be grouped based on the arrangement of nearby fish. The resulting classification and grouped results are shown in Fig. 14. In part (a), $\overline{C_x}$ is plotted against η, and distinct groups of individual fish performance emerge. Specifically, there is a region of multiple high-efficiency fish and a region of higher net force fish. In referencing the geometric positions within the school, groupings are indicated by the results. First, the front fish have no oncoming wake to benefit from, so they have the lowest performance in both η and $\overline{C_x}$, but the $\overline{C_x}$ value is still improved over a solo swimmer due to the block effect. Next, the edge fish have fish on only one side of them and experience a unique anterior body suction, partial block effect, and wall effect. They occupy the highest η region circled in blue, with about a 46% improvement over the front fish. The $\overline{C_x}$ value is around the average for the school. The edge group is further broken down into front-edge, shown in purple, and back-edge, shown in orange. This distinguishes edge fish that have no incident vortices (front-edge) and no block effect (back-edge) from the others. Because of this, the front-edge fish have a lower η, and the back-edge fish have a lower $\overline{C_x}$. Despite this, the edge fish are overall similar and can be combined into a larger group. The middle fish are surrounded by other fish in the school, experiencing full anterior body suction, wall effect, and block effect within the entirety of the group. They show a consistent improvement in $\overline{C_x}$ of about 70% compared to the front fish, but the efficiency of the middle group is lower than the average of the school by about 20%. Finally, the back fish has nothing blocking the flow behind it, subsequently experiencing only anterior body suction, and has about a 50% improvement in η compared to a single fish.

Figures 14(c)–14(f) show the force coefficients and power consumption. They are averaged within each of the spatially motivated groups, and the standard deviations are given by the shaded region. The standard deviation and average for the edge fish show only the top-edge fish, as the bottom edge is a mirror opposite of the top edge.

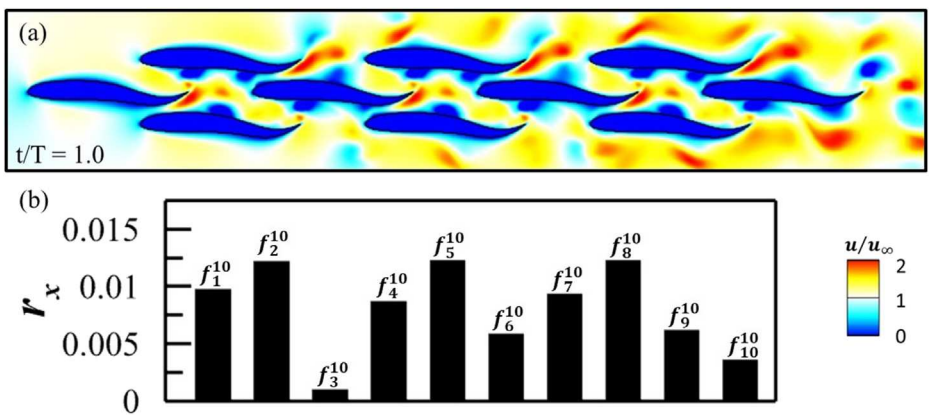

FIG. 13. Normalized x-velocity (a) in the 10-fish school at $t/T = 1.0$, along with the total streamwise momentum in the temporary jet formed behind each fish (b).

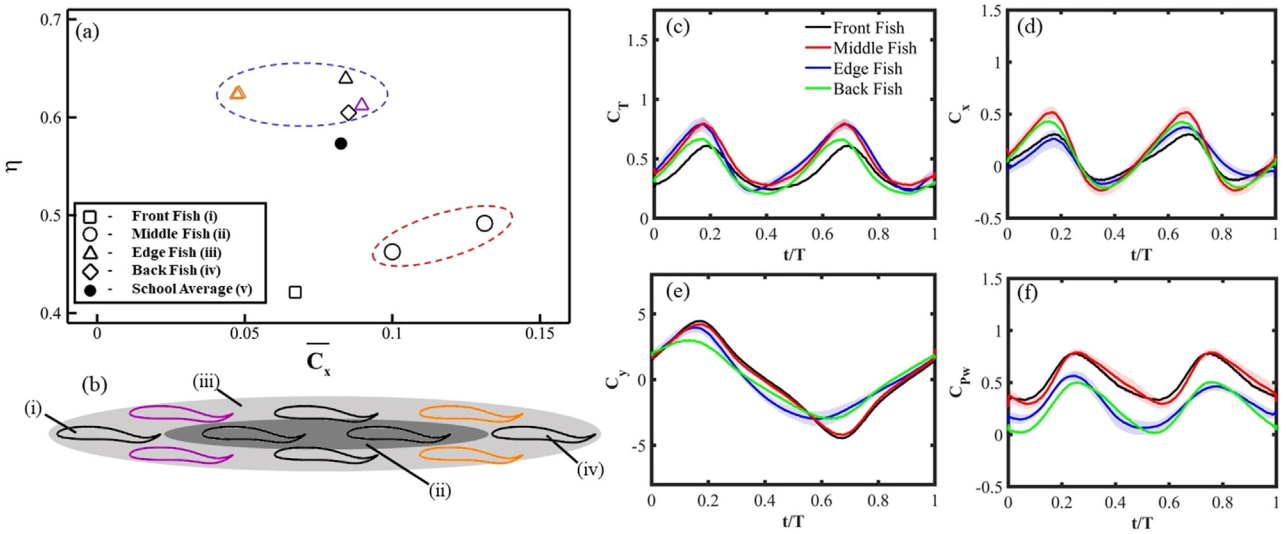

FIG. 14. (a) Cycle-averaged force coefficient vs efficiency in the school by group. (b) Arrangement of baseline school groups, with (i) front fish, (ii) edge fish region, (iii) middle fish region, and (iv) back fish definitions. Front-edge fish (purple) and back-edge fish (orange) are also denoted. C_T (c), C_x (d), C_y (e), and C_{pw} (f) are shown over a cycle of motion. The average for each group is plotted along with the standard deviation for the group. Only the top-edge fish are included for the edge fish.

The cycle-averaged data are provided in Table III. The plots overall show unique and distinctive performance trends within each spatially motivated group. By showing similar trends over a cycle within each group, it is demonstrated that the common fish–fish interaction mechanisms taking place within each group lead to similar performance trends within the group. With these plots, many observations can be made that correspond to the performance groups shown in Fig. 14(a).

First, the front fish, shown in black, demonstrates the lowest C_T (c) and C_x (d), while both the lateral force C_y (e) and the power consumption C_{Pw} (f) are highest for the front fish, which tracks almost exactly as a middle fish. Next, the edge fish, shown in blue, has the highest C_T (c), along with the middle fish, but has a significantly lower C_x (d) compared to the middle and back fish. Interestingly, the peak in C_T is approximately equal in the left and right strokes; however, the right stroke has a higher peak C_x ($t/T = 0.7$), while the left stroke has a higher peak C_y ($t/T = 0.2$). The stroke generating significantly less lateral force is also slightly higher in net force production, due to the anterior body suction. The power consumption is less throughout the cycle compared to the middle and front fish and is lower during the right stroke peak as the tail flaps away from the school than the left. The largest values in C_T (c), C_x (d), and C_y (e) are the middle fish. Subsequently, the power consumption (f) is also highest for the middle fish. Finally, the back fish, shown in green, has a lower C_T (a) than the front and middle, but still maintains a net force near the middle fish values, significantly higher than the edge fish. The lateral forces C_y (d) are significantly lower than other groups, and the power consumption is also lower than the others.

TABLE III. Cycle-averaged performance of groups in 10-fish school, as labeled in Fig. 14(b).

	Front	Middle	Edge	Back
$\overline{C_T^*}$	1.775	2.231	2.233	1.831
$\overline{C_{pw}^*}$	1.9306	1.9392	1.0609	0.9490
$\overline{C_x}$	0.0671	0.1156	0.0738	0.0852
η^*	0.953	1.079	1.414	1.368

1. Effect of Reynolds number

Next, the hydrodynamic interactions and proposed categorization is tested with a variety of Reynolds numbers to observe sensitivity to flow parameters. Note that lower Reynolds numbers in 2D correspond to higher ones in 3D.[42] For this, a single fish and 10-fish school are used, and the Reynolds number increases from 1000 to 2000 and 4000. The school-averaged results are given in Table IV. In the table, a general trend of decreasing thrust while also decreasing power as the Reynolds number increases is seen. This results in a slight increase in efficiency at higher *Re*; however, the benefit over a single fish from schooling maintains around 30% efficiency gain regardless of the change.

Next, the vorticity [(a) and (b)] and cycle-averaged streamwise velocity [(c) and (d)] for the increased Reynolds number is shown in Fig. 15. Overall, the cohesiveness of the vortex structures in the wake declines as the Reynolds number increases. Specific structures in the flow are observed and compared with similar features in Fig. 5. In the front, middle, and back fish, the same vortex trapped inside the channel

TABLE IV. Reynolds number effect on school average performance.

10 − Fish school average	$\overline{C_T^*}$	$\overline{C_{pw}^*}$	$\overline{C_x}$	η^*
$Re = 1000$	2.147	1.312	0.083	1.296
$Re = 2000$	2.076	1.226	0.086	1.311
$Re = 4000$	1.931	1.145	0.087	1.292

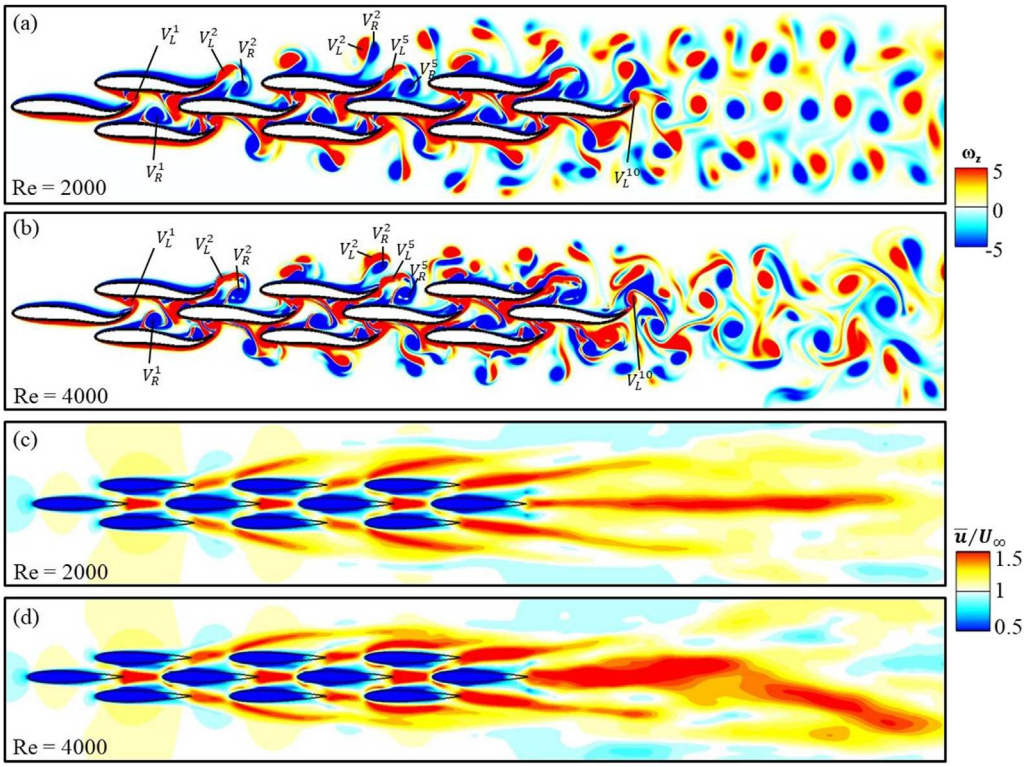

FIG. 15. Vorticity at the peak thrust production (t = 0.18T) for *Re* = 2000 (a) and *Re* = 4000 (b), and cycle-averaged streamwise velocity [(c) and (d)].

is observed in V_L^1 and V_R^1 at all three Reynolds numbers. Because they are fully contained by the channel, there is little opportunity for any change in behavior of the vortex. In the back fish, the same single vortex V_L^{10} is generated; however, it has more interaction with the preceding back-edge fish vortex pair V_R^9 at a higher Reynolds number, where there was previously little interaction between the two. Finally, the edge fish has a similar vortex pair V_L^2 and V_R^2 that is shed from one edge fish and partially interacts with subsequent edge fish for all Reynolds numbers. The cohesiveness of the pair declines significantly at increased Reynolds numbers; however, it is still distinct and has clear interaction with the subsequent edge fish. One major difference comes in the propagation of the edge vortex pair beyond its interaction with the tip of the next edge fish. At the lower Reynolds numbers, the pair propagates laterally into the free stream beside the school, with minimal interaction between the vortex cores and any subsequent body or vortex structure. In the high Reynolds numbers, however, the pair has better adhesion to the body after interacting with the leading-edge, and subsequently interrupts the generation of the next pair, contributing further to the decline in the cohesiveness of the vortex structure. This is demonstrated by V_L^2 and V_R^2, which originated at f_2^{10} during the previous left stroke. In Fig. 15, it is shown to be interrupting the propagation of V_L^5 and V_R^5 downstream. Despite the minor differences, the schematic of primary vortex structures around the body given in Fig. 6 is consistent at higher Reynolds numbers. At *Re* = 2000, there is more lateral deflection in the wake from the wall effect than the baseline, creating a second 2P pair from $f_{5/6}^{10}$ in addition to the 2P pair from $f_{8/9}^{10}$. The short jets behind edge fish diverge more from the center of the school and are longer than the baseline. The long middle jet is narrower, as the lateral spacing between vortices in the rBvK vortex street in the center is reduced. At *Re* = 4000, the wake is narrowed and lacks a consistent coherent structure. The short jets along the edges of the school are similarly longer but directed more in the streamwise direction contrary to *Re* = 2000. Additionally, the long center jet is significantly wider and deflects downwards. The deflection occurs due to the starting of the undulation process creating a lateral deviation of the jet. At the higher Reynolds number, the dipolar structure in the wake is strong enough to decouple from the subsequent vortices in the street, allowing the wake to maintain the asymmetry. This deflection is consistent with previous results of a single undulating body from Zhang *et al.*,[61] which showed that the deflection of the wake occurs in undulating swimmers at increased Reynolds numbers.

The results from utilizing the previously defined groupings are shown in Fig. 16. Once again, the higher η edge fish and higher C_x middle fish zones are immediately apparent at all three Reynolds numbers. The range of values within a group grows with the increase in Reynolds number, even as the groups remain distinct from each other. The back fish have high η and the front fish have the lowest η at all three Reynolds numbers. In the body-averaged values, the standard deviations increase slightly with each increase in Reynolds number. This makes sense, as the vortex structures become less coherent at higher Reynolds numbers the consistency within each group will start to decrease. The continuous coefficients remain distinct from each other, particularly in power consumption. At higher Reynolds numbers, the same overall trends are seen as the 1000 Reynolds number

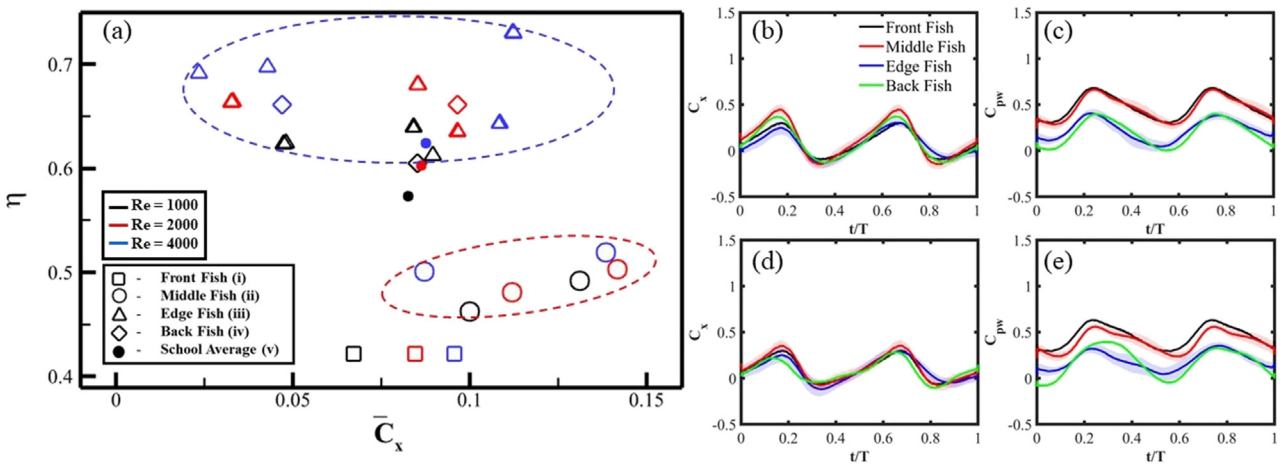

FIG. 16. (a) $\overline{C_x}$ plotted with η for the groupings of a 10-fish school with Reynolds numbers 1000, 2000, and 4000. C_x [(b) and (d)] and C_{Pw} [(c) and (e)] over a cycle of motion by group, with the standard deviation for the group shaded for $Re = 2000$ [(b) and (c)] and $Re = 4000$ [(d) and (e)]. Only the top-edge fish are considered in the average and standard deviation.

TABLE V. School average performance of 16-fish long school.

$\overline{C_T^*}$	$\overline{C_{pw}^*}$	$\overline{C_x}$	η^*
2.467	1.440	0.081	1.319

baseline. Overall, the groupings are shown to be robust within a range of Reynolds numbers. Despite small changes in vortex wakes, the wall effect, block effect, and anterior body suction all remain and are caused by the spatial arrangement of neighboring fish.

2. Increasing of school length and width

Next, the effect of making the school longer is examined by adding two more dense diamond units to the end of the school, resulting in a 16-fish long school. The school-averaged results are shown in Table V. Compared to the 10-fish school, there is an increase in both average thrust production and power consumption, resulting in a slight increase in net efficiency. The vorticity and cycle-averaged streamwise velocity are shown in Fig. 17. The wake behind the school has a wider rBvK vortex street and a corresponding wider long jet in the center. The small jets resulting from the edge fish continue to strengthen as the school gets longer, ending in stronger short jets at the 2P vortex pairs on the edge of the school. In the near-body vortices, the front, middle, and back fish, the same vortex trapped inside the channel is observed in V_L^1 and V_R^1. Because it is fully contained by the channel, there is little opportunity for any change in the behavior of the vortex. In the back fish, the same single vortex V_L^{16} is generated. Finally, the edge fish has a similar vortex pair V_L^3 and V_R^3 that is shed from one edge fish and partially interacts with subsequent edge fish.

The longer school is grouped similarly, and the results are shown in Fig. 18. The same zones of high efficiency and high net force from the edge and middle, respectively, are observed in part (a). The overall spread among C_x in the edge fish is larger, with a bigger drop for the back edge fish than the 10-fish school. In the continuous coefficients of net force and power (c) and (d), the same patterns emerge, with middle fish having the highest net force and power consumption throughout the cycle.

Finally, the effect of making the school wider is examined by adding additional dense diamond sub-units in the spanwise direction, resulting in a 23-fish wide school. The school-averaged results are

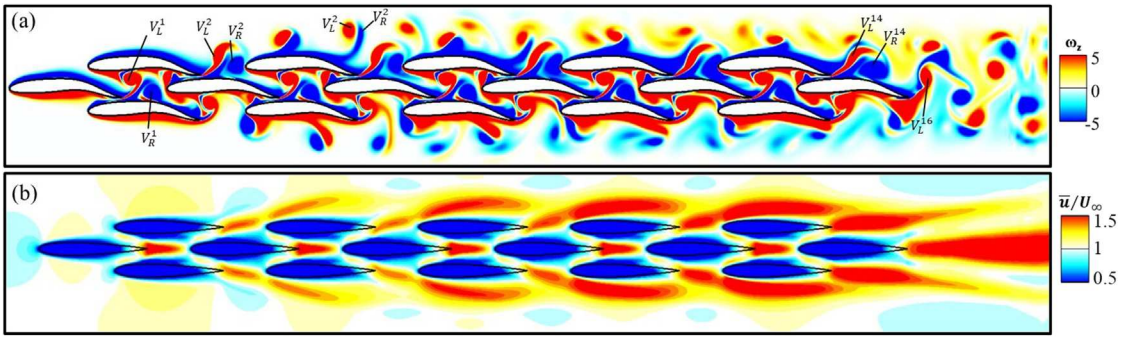

FIG. 17. Vorticity at $t/T = 0.18$ (a) and cycle-averaged streamwise velocity (b) in the 16-fish long school.

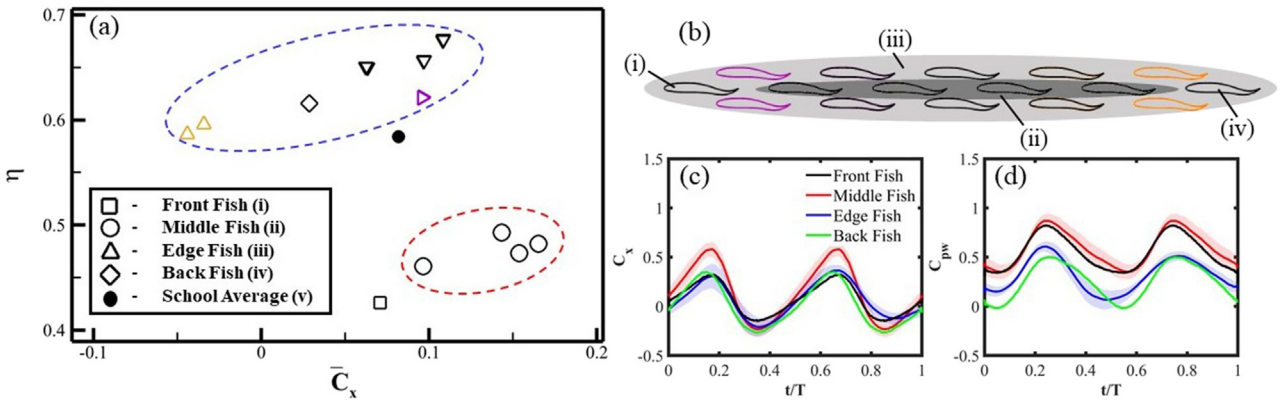

FIG. 18. $\overline{C_x}$ plotted with η for the 16-fish long school (a). Schematic of groupings and arrangement of school (b). C_x (c) and C_{Pw} (d) over a cycle of motion by group, with the standard deviation for the group shaded. Only the top-edge fish are considered in the average and standard deviation.

TABLE VI. School average performance of 23-fish wide school.

$\overline{C_T^*}$	$\overline{C_{pw}^*}$	$\overline{C_x}$	η^*
2.453	1.304	0.062	1.353

shown in Table VI. Compared to the 10-fish school, there is an increase in both average thrust production and power consumption, resulting in a slight increase in the net efficiency; however, C_x is significantly reduced, indicating that the drag on the school has increased. This makes intuitive sense, as the frontal area of the school has increased from $0.4l$ to $0.8l$. The vorticity and cycle-averaged streamwise velocity are shown in Fig. 19. The wake behind the school has flipped to a BvK center, with two pairs of 2P vortex streets neighboring the center street. The inner vortex from the 2P pairs propagates downstream alongside the middle street, creating jets due to the proximity of the opposite sign vortices from each source, resulting in two weaker jets behind the school, occurring between the 2s and 2P wake components. The weaker jets indicate that less momentum is propagated downstream to result in thrust for the fish school. This is reflected in the reduced C_x average compared to the narrower 10 and 16 fish schools. Within the school, near-body vortices remain similar to those observed for the 10-fish school. In the front, middle, and back fish, the same vortex trapped inside the channel is observed in V_L^1 and V_R^1. Because it is fully contained by the channel, there is little opportunity for any change in the behavior of the vortex. In the back fish, the same single vortex V_L^{23} is generated; however, it has destructive interaction with the preceding back-edge fish vortex pair V_R^{21}, where there was previously little interaction between the two. Finally, the edge fish has a similar vortex pair V_L^3 and V_R^3 that is shed from one edge fish and partially interacts with subsequent edge fish.

The wider school is grouped similarly, and the results are shown in Fig. 20. The same zones of high efficiency and high net force from the edge and middle, respectively, are observed in part (a). In the continuous coefficients of net force and power (c) and (d), a similar pattern of highest net force and power consumption is seen in the middle fish. The front fish also has the predicted higher power consumption than the rest of the school.

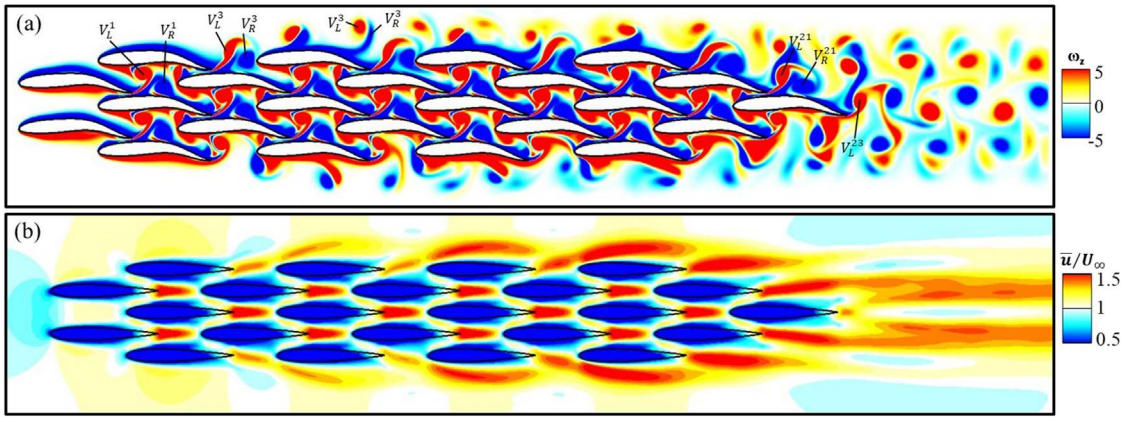

FIG. 19. Vorticity at $t/T = 0.18$ (a) and cycle-averaged streamwise velocity (b) in the 23-fish wide school.

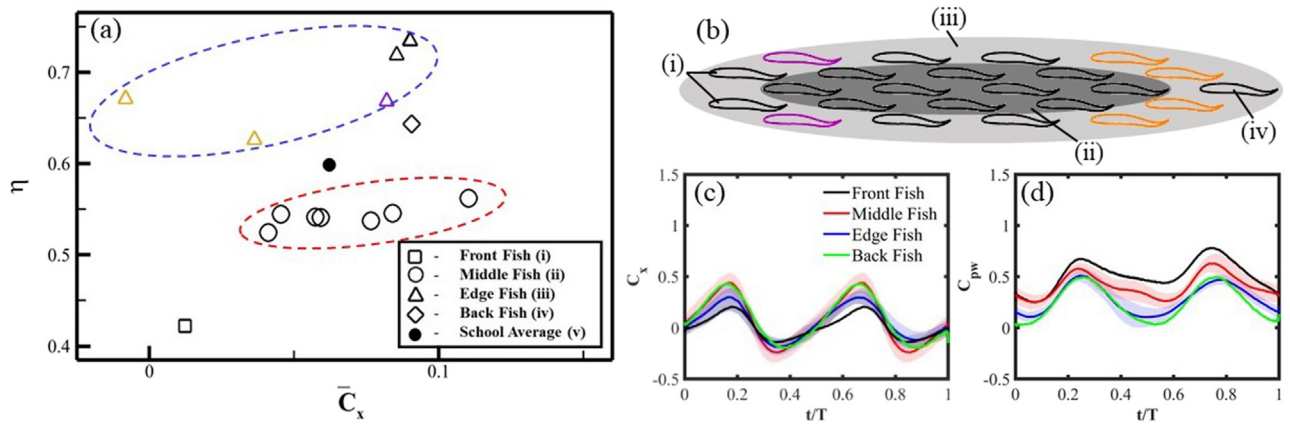

FIG. 20. $\overline{C_x}$ plotted with η for the 23-fish wide school (a). Schematic of groupings and arrangement of school (b). C_x (c) and C_{Pw} (d) over a cycle of motion by group, with the standard deviation for the group shaded. Only the top-edge fish are considered in the average and standard deviation.

IV. CONCLUSION

Utilizing high-fidelity numerical simulations, the in-depth hydrodynamics at play in large planar fish schools are studied. The performance of the fish within the school is found to be significantly improved by swimming within a school rather than alone, and the benefit is further increased in the large school compared to previous studies of smaller schools. The vortex interactions and wake are analyzed, and the enhanced performance of individual fish within the school is shown to be caused by incoming vortex interactions, along with three body–body interaction effects. First, the block effect occurs in the front, edge, and middle of the school, enhancing the thrust production. The wall effect also occurs in the front, edge, and middle of the school and enhances the thrust production at the cost of significant power, except along the edges where the formed vortex pair advects laterally from the school. The anterior body suction effect occurs in the edge, middle, and back of the school and increases thrust production at almost no power cost to the individual. These mechanisms are dependent on the arrangement of the surrounding fish, so intuitive classifications of individual fish are formed based on the position of neighboring fish, categorizing fish into front fish, edge fish, middle fish, and back fish. Hydrodynamic performance of individual fish in large schools shows similar performance between individuals within each group, strengthening the physical basis for the classifications chosen and leading to the major performance zones of the high-efficiency edge fish and the high net force middle fish are predicted, along with the low-efficiency front fish and high efficiency back fish. These mechanisms and groupings are robust to changes in the Reynolds number, length of the school, and width of the school. A limitation of this work is the 2D nature, while real fish schools are 3D. Computational investigation of $n \leq 3$ 3D fish schools have shown persistence of the anterior body suction,[62] block effect, and wall effect[63] mechanisms described in the current study, suggesting that the findings in the 2D large fish schools persist to the 3D analog.

The significance of this work is twofold. First, it offers an initial look into the hydrodynamics of large fish schools using a high-fidelity model, improving on the previous works using a small number of fish or low-order models. In this investigation, the rules for body–body interactions are tested and applied in the setting of a large schools, and previously defined effects are developed to further understanding hydrodynamics in the schools. Finally, from the performance and hydrodynamics of the school, categorizations are elucidated that group the fish with similar performance and interactions. These results are helpful in detailing mechanisms that benefit performance while swimming in large schools, and the groupings provide a useful guidance toward understanding performance and arrangements in fish schools for future studies.

ACKNOWLEDGMENTS

This work was supported by ONR MURI N00014-14-1-0533, ONR MURI N00014-15-1-2234, and NSF CNS-1931929. Additionally, thanks to the University of Virginia Research Computing Group for the availability of the Rivanna supercomputing cluster. The authors would like to thank Jackson Wray for his contribution completing the simulations that motivated this work.

AUTHOR DECLARATIONS

Conflict of Interest

The authors have no conflicts to disclose.

Author Contributions

John Kelly: Conceptualization (equal); Data curation (equal); Formal analysis (equal); Methodology (equal); Validation (equal); Writing – original draft (lead); Writing – review & editing (equal). **Yu Pan:** Conceptualization (equal); Data curation (equal); Formal analysis (equal); Methodology (equal); Writing – review & editing (equal). **Alec Menzer:** Conceptualization (equal); Formal analysis (equal); Writing – review & editing (equal). **Haibo Dong:** Conceptualization (equal); Funding acquisition (equal); Methodology (equal); Project administration (equal); Resources (equal); Software (equal); Supervision (equal); Writing – review & editing (equal).

DATA AVAILABILITY

The data that support the findings of this study are available from the corresponding author upon reasonable request.

REFERENCES

[1]D. Weihs, "Hydromechanics of fish schooling," Nature **241**, 290 (1973).
[2]D. Pavlov and A. Kasumyan, "Patterns and mechanisms of schooling behavior in fish: A review," J. Ichthyol. **40**(2), S163–S231 (2000).
[3]F. Gibouin, C. Raufaste, Y. Bouret, and M. Argentina, "Study of the thrust-drag balance with a swimming robotic fish," Phys. Fluids **30**, 091901 (2018).
[4]C. H. White, G. V. Lauder, and H. Bart-Smith, "Tunabot Flex: A tuna-inspired robot with body flexibility improves high-performance swimming," Bioinspiration Biomimetics **16**, 026019 (2021).
[5]M. Narasimhan, H. Dong, R. Mittal, and S. N. Singh, "Optimal yaw regulation and trajectory control of biorobotic AUV using mechanical fins based on CFD parametrization," J. Fluids Eng. **128**, 687 (2006).
[6]G. V. Lauder, P. Madden, I. Hunter, J. L. Tangorra, N. Davidson, L. Proctor, R. Mittal, H. Dong, and M. Bozkurttas, "Design and performance of a fish fin-like propulsor for AUVs," in Proceedings of 14th International Symposium on Unmanned Untethered Submersible Technology (UUST) (2005), Vol. 1.
[7]H. Kim and D. Kim, "Stability and coupled dynamics of three-dimensional dual inverted flags," J. Fluids Struct. **84**, 18 (2019).
[8]D. Deb, P. Shetty, K. Poddar, and S. Kumar, "Flow induced oscillation of two rigid rectangular plates in a side-by-side configuration," J. Fluids Struct. **99**, 103133 (2020).
[9]T. M. Broering, Y. Lian, and W. Henshaw, "Numerical investigation of energy extraction in a tandem flapping wing configuration," AIAA J. **50**, 2295 (2012).
[10]L. E. Muscutt, G. D. Weymouth, and B. Ganapathisubramani, "Performance augmentation mechanism of in-line tandem flapping foils," J. Fluid Mech. **827**, 484 (2017).
[11]I. Akhtar, R. Mittal, G. V. Lauder, and E. Drucker, "Hydrodynamics of a biologically inspired tandem flapping foil configuration," Theor. Comput. Fluid Dyn. **21**, 155 (2007).
[12]L. Cong, B. Teng, and L. Cheng, "Hydrodynamic behavior of two-dimensional tandem-arranged flapping flexible foils in uniform flow," Phys. Fluids **32**, 021903 (2020).
[13]S. Ramananarivo, F. Fang, A. Oza, J. Zhang, and L. Ristroph, "Flow interactions lead to orderly formations of flapping wings in forward flight," Phys. Rev. Fluids **1**, 071201 (2016).
[14]G. D. Xu, W. Y. Duan, and W. H. Xu, "The propulsion of two flapping foils with tandem configuration and vortex interactions," Phys. Fluids **29**, 097102 (2017).
[15]X. Zhu, G. He, and X. Zhang, "Flow-mediated interactions between two self-propelled flapping filaments in tandem configuration," Phys. Rev. Lett. **113**, 238105 (2014).
[16]G. J. Dong and X. Y. Lu, "Characteristics of flow over traveling wavy foils in a side-by-side arrangement," Phys. Fluids **19**, 057107 (2007).
[17]L. Kang, Z. R. Peng, H. Huang, X. Y. Lu, and W. Cui, "Active external control effect on the collective locomotion of two tandem self-propelled flapping plates," Phys. Fluids **33**, 101901 (2021).
[18]H. Yu, X. Y. Lu, and H. Huang, "Collective locomotion of two uncoordinated undulatory self-propelled foils," Phys. Fluids **33**, 011904 (2021).
[19]M. S. U. Khalid, I. Akhtar, and H. Dong, "Hydrodynamics of a tandem fish school with asynchronous undulation of individuals," J. Fluids Struct. **66**, 19 (2016).
[20]L. Kang, W. Cui, X. Y. Lu, and H. Huang, "Hydrodynamic force induced by vortex-body interactions in orderly formations of flapping tandem flexible plates," Phys. Fluids **34**, 021901 (2022).
[21]J. Deng, X. M. Shao, and Z. S. Yu, "Hydrodynamic studies on two traveling wavy foils in tandem arrangement," Phys. Fluids **19**, 113104 (2007).
[22]A. P. Maertens, A. Gao, and M. S. Triantafyllou, "Optimal undulatory swimming for a single fish-like body and for a pair of interacting swimmers," J. Fluid Mech. **813**, 301 (2017).
[23]M. Saadat, F. Berlinger, A. Sheshmani, R. Nagpal, G. V. Lauder, and H. Haj-Hariri, "Hydrodynamic advantages of in-line schooling," Bioinspiration Biomimetics **16**, 046002 (2021).
[24]A. U. Oza, L. Ristroph, and M. J. Shelley, "Lattices of hydrodynamically interacting flapping swimmers," Phys. Rev. X **9**, 041024 (2019).
[25]S. Alben, "Collective locomotion of two-dimensional lattices of flapping plates. Part 2. Lattice flows and propulsive efficiency," J. Fluid Mech. **915**, A21 (2021).
[26]A. D. Becker, H. Masoud, J. W. Newbolt, M. Shelley, and L. Ristroph, "Hydrodynamic schooling of flapping swimmers," Nat. Commun. **6**, 8514 (2015).
[27]L. Dai, G. He, X. Zhang, and X. Zhang, "Stable formations of self-propelled fishlike swimmers induced by hydrodynamic interactions," J. R. Soc. Interface **15**, 20180490 (2018).
[28]Y. Pan and H. Dong, "Computational analysis of hydrodynamic interactions in a high-density fish school," Phys. Fluids **32**, 121901 (2020).
[29]Y. Pan and H. Dong, "Effects of phase difference on hydrodynamic interactions and wake patterns in high-density fish schools," Phys. Fluids **34**, 111902 (2022).
[30]J. Deng and X. Shao, "Hydrodynamics in a diamond-shaped fish school," J. Hydrodyn., Ser. B **18**, 438 (2006).
[31]S. Y. Chen, Y. H. J. Fei, Y. C. Chen, K. J. Chi, and J. T. Yang, "The swimming patterns and energy-saving mechanism revealed from three fish in a school," Ocean Eng. **122**, 22 (2016).
[32]X. Lin, J. Wu, T. Zhang, and L. Yang, "Self-organization of multiple self-propelling flapping foils: Energy saving and increased speed," J. Fluid Mech. **884**, R1 (2020).
[33]Z. R. Peng, H. Huang, and X. Y. Lu, "Hydrodynamic schooling of multiple self-propelled flapping plates," J. Fluid Mech. **853**, 587 (2018).
[34]S. G. Park and H. J. Sung, "Hydrodynamics of flexible fins propelled in tandem, diagonal, triangular and diamond configurations," J. Fluid Mech. **840**, 154 (2018).
[35]J. Kelly, Y. Pan, and H. Dong, "Wake interactions between groups of undulating foils," in AIAA Scitech 2023 Forum (2023), Vol. 1.
[36]M. Gazzola, A. A. Tchieu, D. Alexeev, A. De Brauer, and P. Koumoutsakos, "Learning to school in the presence of hydrodynamic interactions," J. Fluid Mech. **789**, 726 (2016).
[37]A. Filella, F. Nadal, C. Sire, E. Kanso, and C. Eloy, "Model of Collective Fish Behavior with Hydrodynamic Interactions," Phys. Rev. Lett. **120**, 198101 (2018).
[38]S. S. Killen, S. Marras, J. F. Steffensen, and D. J. Mckenzie, "Aerobic capacity influences the spatial position of individuals within fish schools," Proc. R. Soc. B **279**, 357 (2012).
[39]S. Marras and P. Domenici, "Schooling fish under attack are not all equal: Some lead, others follow," PLoS One **8**, e65784 (2013).
[40]J. J. Videler and F. Hess, "Fast continuous swimming of two pelagic predators, Saithe (*Pollachius Virens*) and Mackerel (*Scomber Scombrus*): A kinematic analysis," J. Exp. Biol. **109**, 209 (1984).
[41]Y. Pan, P. Han, J. Huang, and H. Dong, "Effect of formation pattern on schooling energetics in fish-like swimming," in FEDSM2020, 2020, Vol. 1.
[42]C. K. Hemelrijk, D. A. Reid, H. Hildenbrandt, and J. T. Padding, "The increased efficiency of fish swimming in a school," Fish Fish. **16**, 511 (2015).
[43]M. Daghooghi and I. Borazjani, "The hydrodynamic advantages of synchronized swimming in a rectangular pattern," Bioinspiration Biomimetics **10**, 056018 (2015).
[44]A. Menzer, Y. Gong, F. E. Fish, and H. Dong, "Bio-inspired propulsion: Towards understanding the role of pectoral fin kinematics in manta-like swimming," Biomimetics **7**, 45 (2022).
[45]Y. Pan, W. Zhang, and H. Dong, "Computational modeling and hydrodynamic analysis of fish schools in three-dimensional arrangements," in FEDSM2022, 2022.
[46]P. Han, G. V. Lauder, and H. Dong, "Hydrodynamics of median-fin interactions in fish-like locomotion: Effects of fin shape and movement," Phys. Fluids **32**, 011902 (2020).
[47]J. Kelly, H. Pan, H. Dong, and T. Van Buren, "Wake structures and effect of hydrofoil shapes in efficient flapping propulsion," in FEDSM2021, 2021, Vol. 1.
[48]P. Han, Y. Pan, G. Liu, and H. Dong, "Propulsive performance and vortex wakes of multiple tandem foils pitching in-line," J. Fluids Struct. **108**, 103422 (2022).
[49]J. Kelly, Y. Pan, and H. Dong, "Body shape effects on the hydrodynamic performance of bio-inspired undulating swimmers," in FEDSM2022, 2022, Vol. 1.
[50]M. S. U. Khalid, J. Wang, H. Dong, and M. Liu, "Flow transitions and mapping for undulating swimmers," Phys. Rev. Fluids **5**, 63104 (2020).

[51]J. Kelly, M. S. U. Khalid, P. Han, and H. Dong, "Geometric characteristics of flapping foils for enhanced propulsive efficiency," J. Fluids Eng. **145**, 061104 (2023).
[52]J. Wang, D. K. Wainwright, R. E. Lindengren, G. V. Lauder, and H. Dong, "Tuna locomotion: A computational hydrodynamic analysis of finlet function," J. R. Soc. Interface **17**, 20190590 (2020).
[53]C. Li, H. Dong, and G. Liu, "Effects of a dynamic trailing-edge flap on the aerodynamic performance and flow structures in hovering flight," J. Fluids Struct. **58**, 49 (2015).
[54]W. Zhang, Y. Pan, J. Wang, V. Di Santo, G. Lauder, and H. Dong, "An efficient tree-topological local mesh refinement on cartesian grids for multiple moving objects in incompressible flow," J. Comput. Phys. **479**, 111983 (2023).
[55]R. Mittal, H. Dong, M. Bozkurttas, F. M. Najjar, A. Vargas, and A. von Loebbecke, "A versatile sharp interface immersed boundary method for incompressible flows with complex boundaries," J. Comput. Phys. **227**, 4825 (2008).
[56]P. A. Dewey, D. B. Quinn, B. M. Boschitsch, and A. J. Smits, "Propulsive performance of unsteady tandem hydrofoils in a side-by-side configuration," Phys. Fluids **26**, 041903 (2014).
[57]G. Novati, S. Verma, D. Alexeev, D. Rossinelli, W. M. Van Rees, and P. Koumoutsakos, "Synchronisation through learning for two self-propelled swimmers," Bioinspiration Biomimetics **12**, 036001 (2017).
[58]D. B. Quinn, K. W. Moored, P. A. Dewey, and A. J. Smits, "Unsteady propulsion near a solid boundary," J. Fluid Mech. **742**, 152 (2014).
[59]D. B. Quinn, G. V. Lauder, and A. J. Smits, "Flexible propulsors in ground effect," Bioinspiration Biomimetics **9**, 036008 (2014).
[60]Y. Bao, D. Zhou, J. J. Tao, Z. Peng, H. B. Zhu, Z. L. Sun, and H. L. Tong, "Dynamic interference of two anti-phase flapping foils in side-by-side arrangement in an incompressible flow," Phys. Fluids **29**, 033601 (2017).
[61]D. Zhang, G. Pan, L. Chao, and Y. Zhang, "Effects of Reynolds number and thickness on an undulatory self-propelled foil," Phys. Fluids **30**, 071902 (2018).
[62]S. Verma, G. Novati, and P. Koumoutsakos, "Efficient collective swimming by harnessing vortices through deep reinforcement learning," Proc. Natl. Acad. Sci. USA **115**, 5849 (2018).
[63]K. Yoshida, Y. Ogata, S. Hirai, and K. Hosotani, "Numerical study of the correlation between fish school arrangement and propulsive performance," Artif. Life Rob. **28**, 21 (2023).